RAA 2020 Vol. **20** No. **2**, 18(8pp) doi: 10.1088/1674–4527/20/2/18

http://www.raa-journal.org *http://iopscience.iop.org/raa*

***R**esearch in*
***A**stronomy and*
***A**strophysics*

Synthesising solar radio images from Atmospheric Imaging Assembly extreme-ultraviolet data

Zhuo-Fei Li (李卓霏), Song-Hua Hu (胡松华), Xin Cheng (程鑫) and Ming-De Ding (丁明德)

School of Astronomy and Space Science, Nanjing University, Nanjing 210023, China; *zhuofeili98@gmail.com, xincheng@nju.edu.cn*

Received 2019 May 1; accepted 2019 September 10

Abstract During non-flaring times, the radio flux of the Sun at wavelengths of a few centimeters to several tens of centimeters mostly originates from thermal bremsstrahlung emission, very similar to extreme-ultraviolet (EUV) radiation. Owing to such a proximity, it is feasible to investigate the relationship between the EUV emission and radio emission in a quantitative way. In this paper, we reconstruct the radio images of the Sun through the differential emission measure obtained from multi-wavelength EUV images of the Atmospheric Imaging Assembly on board *Solar Dynamics Observatory* (*SDO*). Through comparing the synthetic radio images at 6 GHz with those observed by the Siberian Radioheliograph, we find that the predicted radio flux is qualitatively consistent with the observed value, confirming thermal origin of the coronal radio emission during non-flaring times. The results further show that the predicted radio flux is closer to the observations in the case that includes the contribution of plasma with temperatures above 3 MK than in the case of only involving low temperature plasma, as was usually done in the pre-*SDO* era. We also discuss applications of the method and uncertainties of the results.

Key words: Sun: radio radiation — Sun: atmosphere — Sun: UV radiation

1 INTRODUCTION

Solar extreme-ultraviolet (EUV) radiation refers to electromagnetic radiation at the wavelengths of 100–1200 Å. It is of thermal origin and generated mainly through line emission of highly ionised ions, whose intensity depends on the plasma temperature and density, or more precisely the emission measure (EM) (Zhang et al. 2001). On the other hand, solar radio emission usually includes incoherent emission and coherent emission. Thermal bremsstrahlung and gyroresonance emission of free electrons are incoherent emission, while the coherent emission results from nonthermal electrons, including electron cyclotron maser emission, plasma emission, etc. (Kundu 1965). Bremsstrahlung originates from free-free emission through Coulomb collisions between electrons and ions (Wild et al. 1963). The emission flux from bremsstrahlung is also dependent on the plasma EM, similarly to the EUV emission. By contrast, gyroresonance emission is generated by non-relativistic electrons in magnetic fields, whose flux is thus not only dependent on the EM but also on the magnetic field. For both the EUV and radio radiations, their temporal evolution generally includes two components: a slowly varying component (the background) from the quiet Sun and an impulsively varying one from flares in active regions (Kundu 1965). For active regions, in non-flaring periods, the EUV flux is almost always dominated by thermal bremsstrahlung emission, while the radio flux is also mostly from bremsstrahlung with some possible contribution from non-thermal gyroresonance emission. However, for quiescent regions, EUV and radio emissions are almost fully contributed by bremsstrahlung as the magnetic field there is very weak so that the gyroresonance emission can be ignored (Shibasaki et al. 2011).

Because of the similar origin for EUV and radio emissions in non-flaring times, a quantitative comparison between them can help diagnose the physical properties of the corona. Using data from the Extreme ultraviolet Imaging Telescope (EIT) and assuming a corona with two temperature components in the range of 0.5–3 MK, Zhang et al. (2001) determined the EM of each pixel over the full disk for the hot and cool components. They further calculated the brightness temperature (T_b) of radio emission by applying the formula

$$T_b = 0.2\nu^{-2}T_C^{-0.5}EM_C + 0.2\nu^{-2}T_H^{-0.5}EM_H\,, \quad (1)$$

where ν denotes the frequency in the radio domain, and T_C (T_H) and EM_C (EM_H) are the temperature and EM of the cool (hot) plasma component, respectively. Note that the formula is valid only if the emission is optically thin, i.e., the optical depth (τ) is much smaller than 1. As a result, they found that the predicted and observed Very Large Array (VLA) radio images exhibit very similar morphologies, and a good linear correlation exists between the predicted brightness temperature and the observed one. However, they also noted that the predicted flux is systematically larger than the observed one, which was attributed to an underestimation of the abundance of iron relative to hydrogen when calibrating the EIT data.

Nevertheless, with the launch of *Solar Dynamics Observatory* (*SDO*; Pesnell et al. 2012), it was realised that the coronal plasma is actually distributed in a very wide temperature range. In particular, for flaring active regions, the temperature range could be 0.5–20 MK (e.g., Cheng et al. 2012; Hannah & Kontar 2012; Cheung et al. 2015). Even during non-flaring times, the emission from plasma with temperatures of above 3 MK is still nontrivial (e.g., Hannah et al. 2016; Grefenstette et al. 2016). This means that the hot plasma could also have a considerable contribution to the radio emission, especially in the radio wavelength range of centimeters to several tens of centimeters. It is thus more reasonable to include the entire thermal plasma in the corona to predict the radio emission. In this paper, by employing data from the Atmospheric Imaging Assembly (AIA; Lemen et al. 2012), we calculate the differential emission measure (DEM) for of each pixel over the full disk, with which a map of T_b is estimated under the assumption of an optically thin corona. The main purpose is to revisit the relationship between the predicted radio emission and the observed one during non-flaring times. The observational data and analytical procedure are introduced in Section 2, which is followed by the results in Section 3. A summary and discussions are given in Section 4.

2 DATA SELECTION AND ANALYSES

The AIA on board *SDO* observes the Sun's atmosphere in seven EUV channels, six of which, centered at 94 Å, 131 Å, 171 Å, 193 Å, 211 Åand 335 Å, are utilized for DEM analysis. Each AIA EUV image contains 4096 by 4096 pixels with a spatial resolution of 1.2″, covering a field of view of 1.3 $R_\odot$. The time cadence of the images is 12 s. These data can be freely downloaded from the *SDO* website[1].

Full disk radio images are provided with the Siberian Radioheliograph (SRH), which was constructed as an upgrade of the Siberian Solar Radio Telescope (SSRT). It observes the Sun at 5.7 GHz in routine mode but switches to a special mode for high-cadence and high-resolution observations when solar radio bursts are detected (Grechnev et al. 2003). SRH started routine observations in August of 2016 at several frequencies in the range of 4–8 GHz with an angular resolution of 1′–2′ and a cadence of about 12 s (Lesovoi et al. 2012). Here, we consider the full disk radio images at 6.0 GHz observed on 2016 March 16 for analysis.

We also utilize the 17 GHz radio images that were recorded by Nobeyama Radioheliograph (NoRH). NoRH provides one full disk image every second at two frequencies of 17 and 34 GHz, and began operation in June of 1992. The spatial resolution is about 10″ at 17 GHz and 5″ at 34 GHz. The images are reconstructed through the CLEAN algorithm (Nakajima et al. 1994). The 17 GHz full disk image that was acquired on 2016 March 16 was downloaded from the NoRH homepage[2].

In order to predict the parameter T_b at each pixel over the full disk, we need to first determine the DEM at this pixel as a function of temperature. Theoretically, for an optically thin medium, the EM is defined as

$$EM = \int n_e(s) n_H(s) ds \,, \tag{2}$$

where n_e is the electron number density, n_H is the hydrogen number density and s is the depth along the line of sight. The DEM is

$$DEM(T) = \frac{dEM}{dT} = \int \frac{dn_e(s) n_H(s)}{dT(s)} ds \,. \tag{3}$$

The EUV intensity at a specific passband i can be expressed as

$$I_i = \int R_i(T) DEM(T) dT \,, \tag{4}$$

where $R_i(T)$ is the temperature response function of the AIA detector at this passband. With the observed EUV images at the six passbands, the DEM at each pixel can be derived through resolving an inverse problem even though it is ill posed. The nonlinear response functions make the inversion very complicated. Here, we adopt the code developed by Cheung et al. (2015), which implements a matrix inversion to ensure non-negative solutions. The code seeks a solution with an optimal error resolution and the computation is faster than previous DEM inversion methods. Thus, it is very appropriate for the present project. Note that in this work, we do not need to know the exact values of n_e and n_H, but just deduce the DEM value in order to quantify the brightness temperature as written below.

After knowing DEM, the brightness temperature can be predicted at a given frequency. The optical depth τ of

[1] `http://jsoc.stanford.edu/ajax/exportdata.html`

[2] `https://solar.nro.nao.ac.jp/norh/`

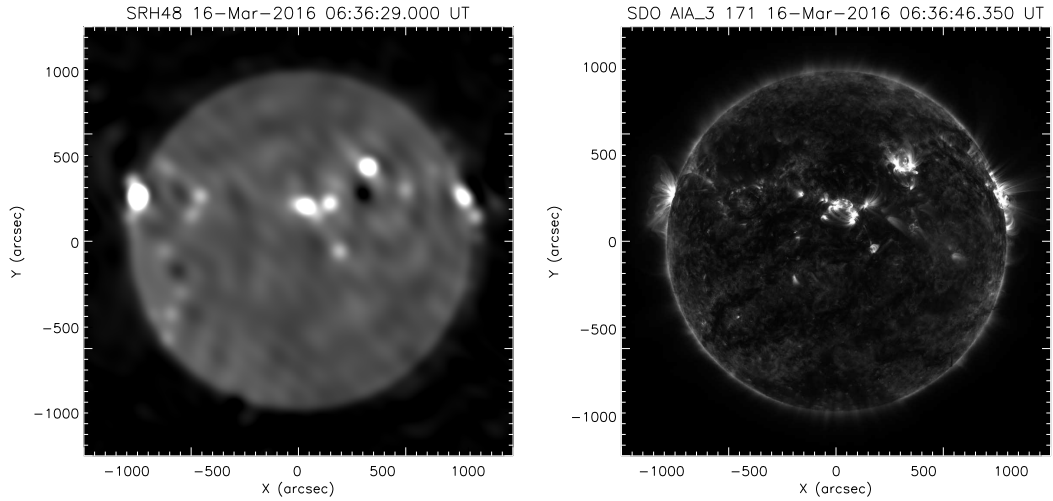

Fig. 1 *Left*: Full disk 6 GHz radio image on 2016 March 16 observed by SRH. *Right*: Corresponding full disk EUV image observed by AIA at the 171 Å passband at a closest time.

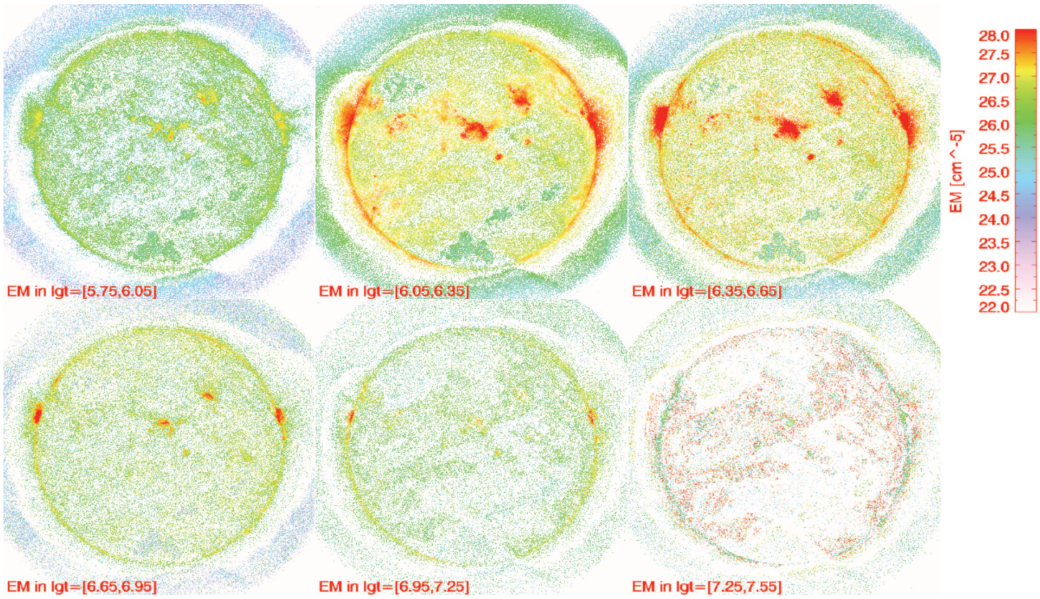

Fig. 2 EM maps at different temperature intervals.

thermal bremsstrahlung is proportional to the EM and is also a function of the electron temperature T_e and the frequency ν. At radio wavelengths, where the Rayleigh-Jeans limit is valid, it is reasonable to quantify radio flux with T_b (Zhang et al. 2001), which can then be expressed as

$$T_b = \int_{T_{\min}}^{T_{\max}} 0.2\nu^{-2}T^{-1/2}DEM(T)dT\,. \qquad (5)$$

In the current work, the temperature is integrated over the range 0.5–10 MK, where the DEM solutions have been tested and are relatively reliable (e.g., Cheng et al. 2012).

3 RESULTS

The full disk solar radio image at 6 GHz on 2016 March 16 observed by SRH is displayed in the left panel of Figure 1. For comparison, the AIA EUV image at the 171 Å passband at the same time is featured in the right panel of Figure 1. One can see that the locations with strong radio emission correspond to the active regions that can be clearly identified with enhanced 171 Å emission very well. However, the radio image is much more blurry than the 171 Å image, which is mainly due to the fact that the latter has a much higher spatial resolution (1.2″) than the former (9.6″).

To reconstruct the radio images from the EUV data, we first calculate the DEM at each pixel of the full disk

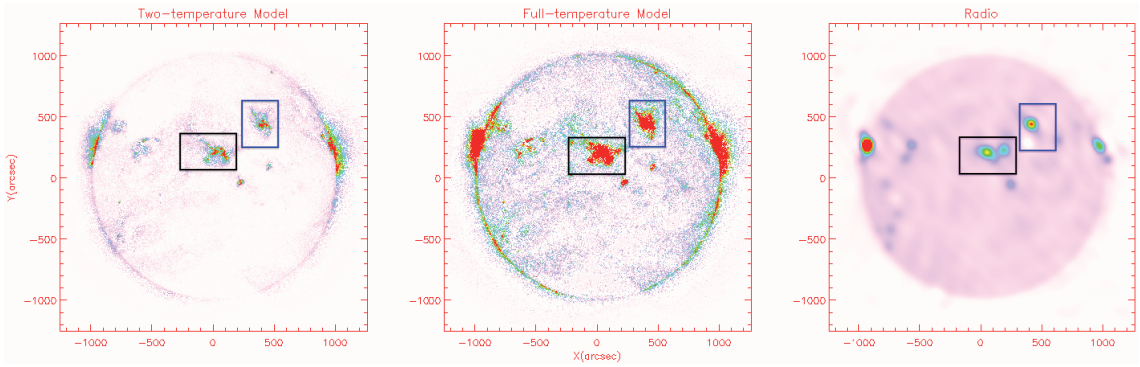

Fig. 3 *Left*: Predicted T_b image of the full solar disk at 6 GHz calculated by the two-temperature model. Middle: Predicted T_b image at 6 GHz from the full-temperature model. *Right*: Observed radio image at 6 GHz from SRH. The two *boxes* indicate the NOAA Active Regions 12519 (*black*) and 12521 (*blue*).

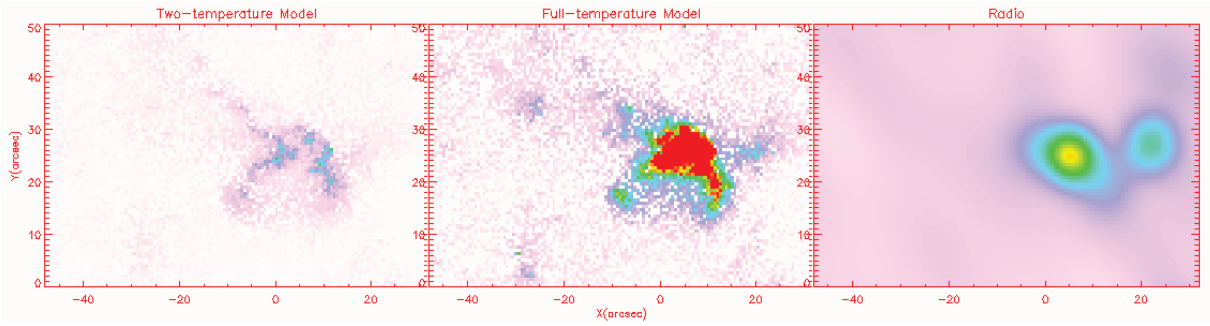

Fig. 4 Same as Fig. 3 but for NOAA Active Region 12519 located at the disk center.

using six AIA EUV passbands. Here, the AIA images are degraded to the same resolution and can thus be directly compared with the radio data. The temperature range is set as $5.7 \leq \log T \leq 7.7$ with an interval of $\Delta \log T = 0.1$, corresponding to 0.5–5 MK.

In Figure 2, we depict the EM maps of the full disk at the different temperature intervals. We can see that the emission in active regions is primarily from the plasma in the temperature range of 1–5 MK. The EM map at the temperature interval of $7.2 \leq \log T \leq 7.5$ manifests a lot of high EM points (in red), which turn out to be incorrect after a careful inspection of the corresponding DEM curves. Thus, we restrict the temperature range to be less than $\log T = 7.0$ when calculating the EM and then T_b following Equation (5). In order to compare our results with those of Zhang et al. (2001), we also calculate the parameter T_b using the two-temperature model they proposed, in which the cool component has a temperature range from 0.8 MK to 1.4 MK, and the hot one is from 1.6 MK to 2.8 MK. In the following, we also integrate over temperature range of 0.5–10 MK, which is called the full-temperature model. A comparison between the two models can help reveal how much contribution is from the plasma above the temperature of 3 MK to the thermal radio emission.

Through Equations (1) and (5), we reconstruct the T_b image of the full disk at 6 GHz as shown in Figure 3. One can see that the locations of active regions in the reconstructed images are basically consistent with those in the observed images. However, the predicted images from the full-temperature model seem to show more structures and stronger emission than the images from the two-temperature model, which can be more apparently revealed in the selected NOAA Active Region 12519 as displayed in Figure 4 (also marked with a black box in Fig. 3). This active region just appears as an oval shape in the observed radio image but exhibits two branches extending toward the south in the predicted image. With the same contrast, the full-temperature model manifests the structures in active regions more clearly and displays a T_b distribution at the center of the active region, which is more consistent with observations. It suggests that the full-temperature model is better at estimating the radio emission from EUV observations.

For the purpose of quantitatively investigating the relationship between the predicted T_b and observed one, we generate scatter plots, together with linear fitting to the data, for all the pixels in the full disk and the selected active region. The T_b values for most pixels from both the predicted and observed images are very small, even close

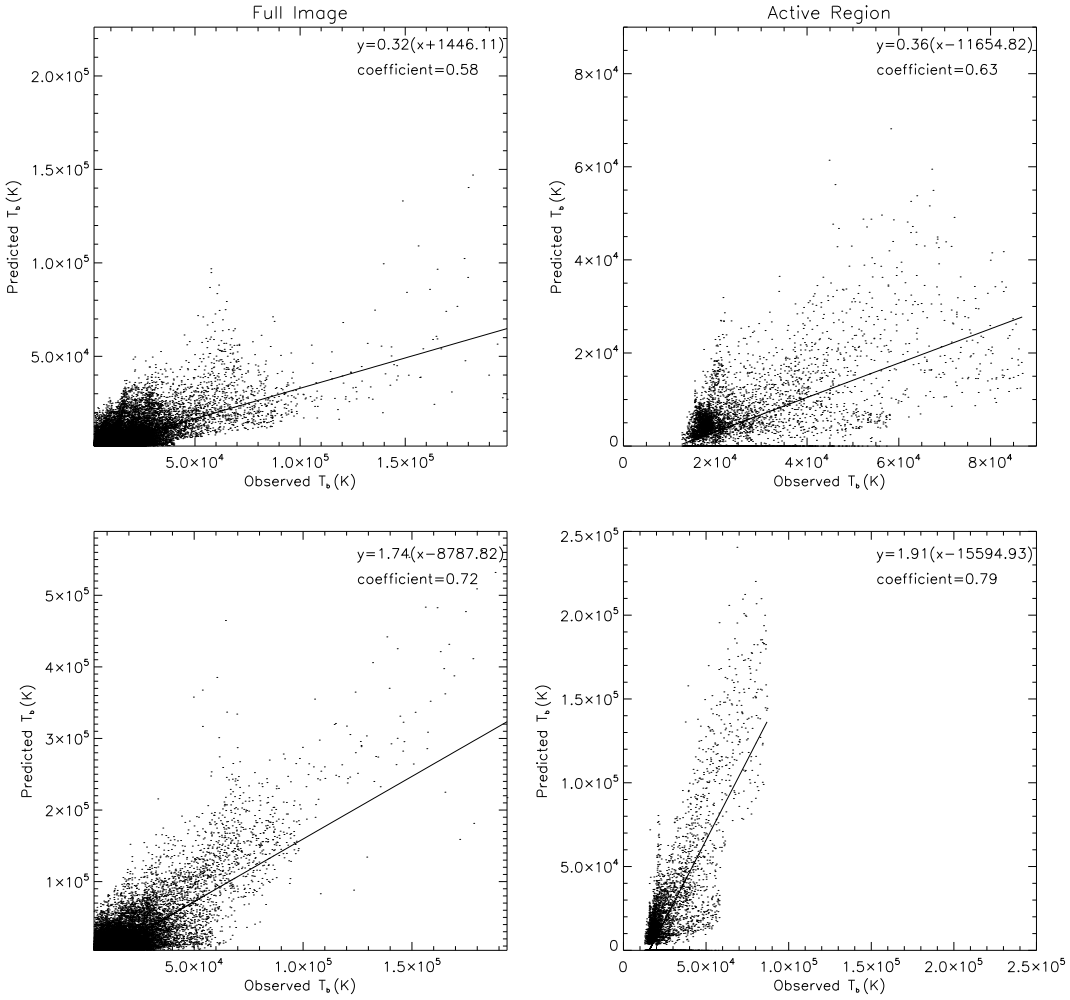

Fig. 5 Pixel-by-pixel correlation plots between the predicted T_b at 6 GHz from the two-temperature model and the observed one for the full disk (*upper left*) and a selected active region (*upper right*). The *solid lines* represent the linear fitting to the data points. The fitting formulas and correlation coefficients are also indicated in each panel. Lower: The correlation results between the full-temperature model and the observed value are also displayed for the full disk (*lower left*) and the active region (*lower right*).

to zero, which were thought to be unreasonable, and thus are removed. In the two-temperature model, pixels whose values are less than 2000 K are removed, and in the full-temperature model, the boundary is 4000 K. The results are presented in Figure 5. One can see that the two-temperature model predicts the T_b value at 6 GHz roughly in a linear relationship with the observed one, for both the full disk (upper left panel of Fig. 5) or a specific active region (upper right panel of Fig. 5). The linear correlation coefficients are found to be 0.58 and 0.63 for the full disk and the active region, respectively. Moreover, it is found that for the full disk, the predicted T_b is mostly distributed in the range of 1000 K–0.1 MK, which is systematically smaller than the observed one as revealed by the slopes of the fitted lines, 0.32 and 0.36. Interestingly, when inspecting the results from the full-temperature model, we find that the correlations between the predicted T_b and observed one become better for both the full disk and the active region (lower left and lower right panels of Fig. 5 respectively). The corresponding linear correlation coefficients are 0.72 and 0.79, respectively. However, in this case the predicted T_b is systematically larger than the observed one. The slopes of the fitted lines are 1.74 and 1.91 for the full disk and the active region, respectively. Note that the best fitting requires non-zero constants to be added to or subtracted from the observed value of T_b. These constants in the fitting functions may result from the deconvolution process when making radio images. The above results show that the full-temperature model may be more accurate than the two-temperature one in predicting the radio emission of thermal origin and that the radio emission at low frequencies is mostly dominated by emission from the thermal plasma.

We also apply the same analysis to NOAA Active Region 12521 (marked with blue box in Fig. 3) and derive a good linear correlation between the predicted and

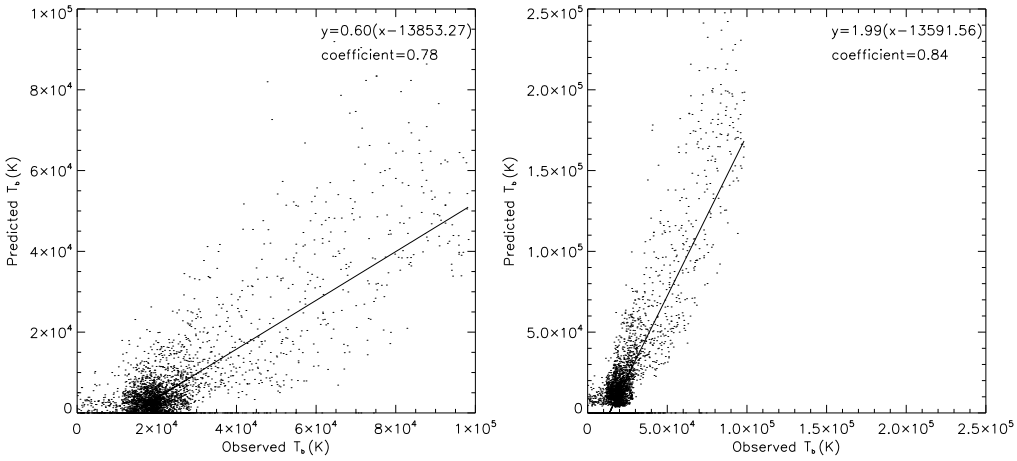

Fig. 6 Pixel-by-pixel plots for NOAA Active Region 12521 showing a good linear correlation between the predicted and observed T_b. *Left*: The correlation results between the two-temperature model and the observed value. *Right*: The correlation results between the full-temperature model and the observed value.

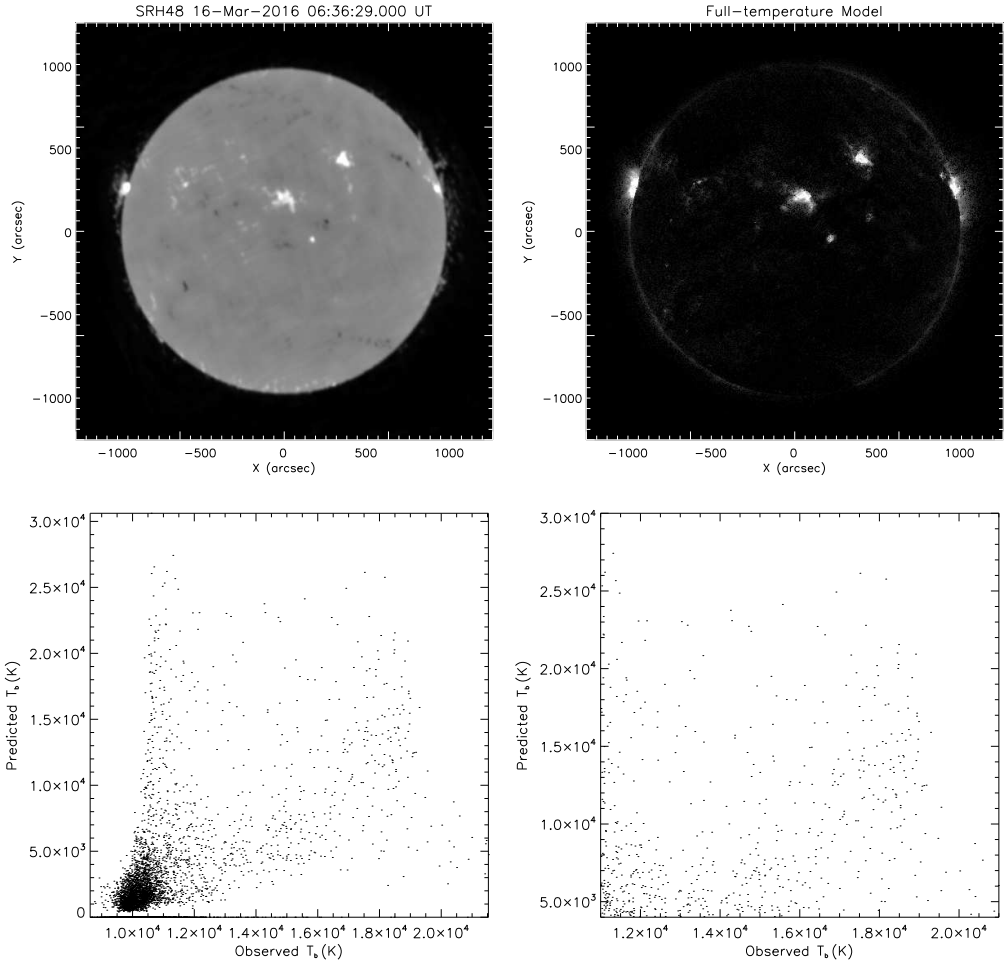

Fig. 7 NoRH full disk radio image at 17 GHz observed on 2016 March 16 (*upper left*) and the predicted radio image from the full-temperature model at the same frequency and the same time (*upper right*). Pixel-by-pixel correlation plots between the predicted T_b and the observed one for the full disk (*lower left*). The *lower right* panel depicts an enlarged region of the lower left panel in the high T_b range.

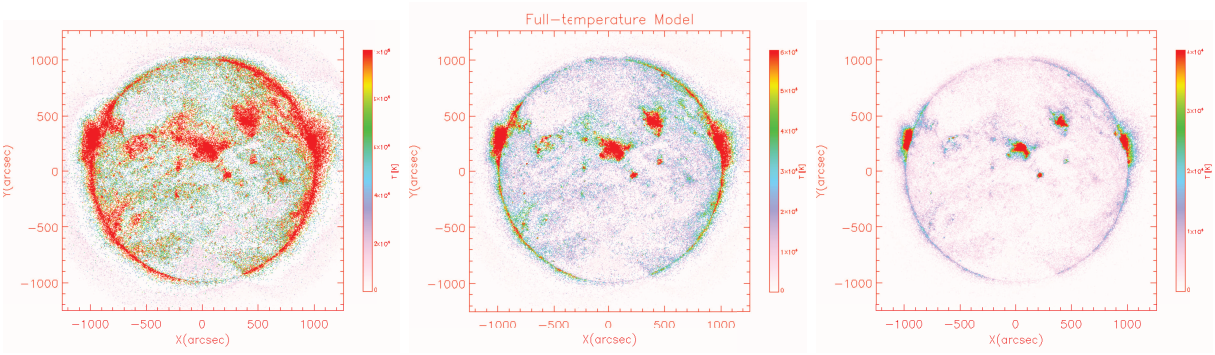

Fig. 8 Predicted full disk T_b maps at 2.0, 4.0 and 8.0 GHz on 2016 March 16.

observed T_b (Fig. 6). In addition, we analyse the full disk without any active regions, and find that the correlation becomes very bad, so we conclude that during non-flaring period, the radio emission in the active region mainly comes from thermal bremsstrahlung emission. Of course, the gyroresonance emission should also have a contribution to the observed T_b, and could be one of the main reasons for the discrepancy between the predicted T_b and the observed one.

In a previous study, Zhang et al. (2001) also concluded that the predicted radio emission is systematically stronger than the observed value by a factor of 2.0. This work, when implementing the same two-temperature model as in Zhang et al. (2001), obtains a much lower predicted value, about 0.36 times the observed one. Such a great difference may be caused by two reasons: the first is that Zhang et al. (2001) did not include the contribution of plasma with temperatures above $\sim$ 3 MK; the second is an underestimation of the iron abundance in their work. The abundance of iron relative to hydrogen for EIT calibration is set to be 3.9×10^{-5}, while that for the AIA calibration is 1.26×10^{-4} (Meyer 1984; Schmelz et al. 2013). We also tentatively study the relationship between the predicted T_b at high frequencies and the observed one. In the upper panels of Figure 7, we show one full disk image at 17 GHz from NoRH and the predicted T_b image at 17 GHz from the full-temperature model. It is found that for quiescent regions, the predicted T_b is much lower than the observed value. For active regions, although the predicted T_b image exhibits a very similar morphology to the observed one, their quantitative correlation displayed in the scatter plot is really bad as revealed in the lower panels of Figure 7. Considering the fact that there are few non-thermal particles during non-flaring periods, we think that the radio emission at high frequencies should probably be the gyrosynchrotron emission of the thermal electrons in hot plasma with a relatively strong magnetic field. This is the likely reason for the discrepancy between the predicted and observed values of T_b.

As shown above, there is generally a good linear relationship between the predicted radio T_b at low frequencies, derived from the multi-passband EUV data, and the observed one. We also try to predict the T_b maps at other frequencies. In Figure 8, we calculate three T_b maps at 2.0, 4.0 and 8.0 GHz, respectively, which can be compared with real observations at a wider frequency range such as that from the Mingantu Spectral Radioheliograph (MUSER) (Yan et al. 2016) in the near future. We are planning to calculate the T_b maps at four frequencies of 1, 2, 4 and 8 GHz one day per week starting from 2016 May 16. All data, also including the DEM results, are open to the public and can be downloaded at the website of the project[3].

4 SUMMARY AND DISCUSSIONS

In this paper, we revisit the relationship between the predicted radio images derived through a two-temperature model and a full-temperature model and the observed radio images during non-flaring times. It is found that the full-temperature model is better at reproducing the observational radio intensity, in particular for active regions. The results confirm that the radio emission of the quiet Sun at low frequencies primarily originates from thermal plasma in the corona, thus presenting the potential for reconciling with MUSER observations in the near future.

However, we also find that the predicted T_b at each pixel does not exactly equal the observed one; the former is usually larger than the latter if using the full-temperature model. Such a discrepancy could be due to the uncertainties in the DEM resolutions derived from the AIA EUV intensities. Note that an inaccurate absolute calibration of radio images could also make the observed flux deviate from the predicted one. Moreover, the predicted radio emission in the full-temperature model is obviously larger than the observed values in the two-temperature model. A possible reason is that the EM of the plasma in the full-temperature

[3] `https://pan.baidu.com/s/1L5kti-oz6z8cXnnZN1ic7w`

model is overestimated. That is to say, an accurate determination of the DEM together with a precise abundance of iron is essential in properly predicting the radio emission. In addition, the gyroresonance emission from thermal electrons can also give rise to a discrepancy between reconstructed T_b from the EUV emission and the observed one.

Acknowledgements We are grateful to the referee for constructive comments that helped improve the paper. Z. F. L., S. H. H., X. C. and M. D. D. are supported by the National Natural Science Foundation of China (Grant Nos. 11722325, 11733003, 11790303 and 11790300), and by the Jiangsu Natural Science Foundation (BK20170011). X. C. is also supported by the "Dengfeng B" program of Nanjing University.

References

Cheng, X., Zhang, J., Saar, S. H., & Ding, M. D. 2012, ApJ, 761, 62

Cheung, M. C. M., Boerner, P., Schrijver, C. J., et al. 2015, ApJ, 807, 143

Grechnev, V. V., Lesovoi, S. V., Smolkov, G. Y., et al. 2003, Sol. Phys., 216, 239

Grefenstette, B. W., Glesener, L., Krucker, S., et al. 2016, ApJ, 826, 20

Hannah, I. G., & Kontar, E. P. 2012, A&A, 539, 146

Hannah, I. G., Grefenstette, B. W., Smith, D. M., et al. 2016, ApJ, 820, 14

Kundu, M. 1965, Solar Radio Astronomy (Interscience: New York)

Lemen, J. R., Title, A. M., Akin, D. J., et al. 2012, Sol. Phys., 275, 17

Lesovoi, S. V., Altyntsev, A. T., Ivanov, E. F., & Gubin, A. V. 2012, Sol. Phys., 280, 651

Meyer, J.-P. 1985, ApJS, 57, 173

Nakajima, H., Nishio, M., Enome, S., et al. 1994, IEEE Proceedings, 82, 705

Pesnell, W. D., Thompson, B. J., & Chamberlin, P. C. 2012, Sol. Phys., 275, 3

Schmelz, J. T., Jenkins, B. S., & Kimble, J. A. 2013, Solar Physics, 283, 325

Shibasaki, K., Alissandrakis, C. E., & Pohjolainen, S. 2011, Sol. Phys., 273, 309

Wild, J. P., Smerd, S. F., & Weiss, A. A. 1963, ARA&A, 1, 291

Yan, Y., Chen, L., & Yu, S. 2016, IAUS, 20, 427

Zhang, J., Kundu, M. R., White, S. M., Dere, K. P., & Newmark, J. S. 2001, ApJ, 561, 396